



The reliability assessment of Au–Al bonds using parallel gap resistance microwelding

Peng Liu¹ · Sen Cong² · Xingwen Tan² · Xiang Lin¹ · Ping Wu¹ 

Received: 7 January 2020 / Accepted: 27 February 2020 / Published online: 5 March 2020
© Springer Science+Business Media, LLC, part of Springer Nature 2020

Abstract

The Au–Al bonding joint was prepared by the parallel gap resistance microwelding. The microstructural evolution of Au–Al bonds was investigated under thermal aging, and the mechanical properties of Au–Al intermetallic compounds (IMCs) were computed by the first-principles calculations. We found that the Au–Al IMCs along with cracks grew during aging time and temperature increasing. The formation of the cracks is explained by the Kirkendall effect, volumetric shrinkages and thermal mismatch. Based on the experimental data, the growth of the IMCs is fitted to the diffusion equation to describe the performance degradation of Au–Al bonds. The Arrhenius relationship is introduced as the acceleration model to describe the effects of thermal stress on lifetime. Furthermore, the Weibull–Arrhenius model is built by the combination of the Weibull distribution and the Arrhenius relationship, which provide a method to estimate the lifetime distribution under work condition.

1 Introduction

Compared with tape-automated bonding and flip chip bonding, wire bonding technology is used extensively in chip interconnection filed because of its cost effectiveness [1]. Wire bonding can be divided into thermal compression bonding, ultrasonic bonding and thermosonic bonding. However, with the miniaturization of electronic packaging, new challenges have emerged in integrated circuit packaging technology, such as the increase in I/O numbers, reduction in bond pad pitch and emergence of alloyed gold wires and copper wires [2–5]. Recently, the parallel gap resistance microwelding, which is a high-speed solid-state welding process, came into the sight of researchers owing to its short heating time, thermal concentration, and convenient and suitable interconnection for dissimilar materials [6].

Sharma et al. [7] studied parallel gap welding of precious metal (Au, Ag, Pt) wires on thick gold substrates in micro-electromechanical systems and analyzed the effects of welding voltage, duration, electrode gap and welding pressure on the strength of joints. Liu et al. [6] investigated the main parameters (welding voltage, welding time and electrode force) as well as the mechanical properties of the Cu wire/Au plating joints using parallel gap resistance microwelding process. Simultaneously, this technology was widely applied in the interconnection between wire and coating in solar battery, sensors, relays and medical devices [8–10].

Nevertheless, these researches were mainly aggregated on the welding process rather than the properties of bonding joints. The reliability of bonding joint plays a vital role in the normal operating of devices. The miniaturization is still a key design tendency in electronics industry [11], meaning that a large amount of Joule heat generated in devices is still the momentous failure factor in the interconnection between wire and chips. It is essential to investigate the failure mechanism of bonds under thermal stress. Besides, the lifetime of electronic equipment is usually limited by the failure of bonding joints. From the experimental data, we established the stress-lifetime relationship to estimate the reliability of the bonding joints.

✉ Sen Cong
congse305@163.com

✉ Ping Wu
pingwu@tju.edu.cn

¹ Tianjin Key Laboratory of Low Dimensional Materials Physics and Preparing Technology, Department of Applied Physics, Faculty of Science, Tianjin University, Tianjin 300354, People's Republic of China

² Institute of Electronic Engineering, China Academy of Engineering Physics, Mianyang 621900, People's Republic of China

2 Experimental

The Al wire (diameter of 100 μm) was bonded on the Au pad (thickness of 3 μm) using parallel gap resistance microwelding. The welding current, time and electrode force are 200 A, 5 ms and 10 N, respectively. Each sample containing 6 bonding joints was manufactured under the same process. 12 samples were aged at 100 $^{\circ}\text{C}$, 125 $^{\circ}\text{C}$ and 150 $^{\circ}\text{C}$ for 24 h, 120 h, 240 h and 360 h, respectively, with one sample as the control group. The microstructures of bonding joints were examined by SUPRA 55VP Scanning Electron Microscope (SEM), and the compositions of the materials were confirmed by the energy-dispersive X-ray (EDX). The thickness of IMCs layer was measured using Adobe Photoshop CS 5.0 software. The first-principles calculations were implemented with Vienna Ab-initio Simulation Package (VASP) codes [12]. For exchange correlation energy, the generalized gradient approximation (GGA) of Perdew–Burke–Ernzerhof (PBE) was chosen [13]. The Methfessel-Paxton technique with 0.1 eV smearing determined the electronic occupancies. The accuracy of energy convergence was set as 5×10^{-6} eV/atom and the valence electron configurations of Au and Al were $5d^{10}6s^1$ and $2s^23p^1$, respectively.

3 Results and discussion

3.1 Evolution of intermetallic compounds

Figure 1 shows two typical regions on the interface of the initial Au–Al bonds. The upper part of black area and the lower part of gray area are Cu phase and Al phase, respectively. The distinct part in the middle is the Au layer. In Fig. 1a, the Au layer is subjected to tremendous deformation and the thickness is compressed to less than 1 μm due to the

high pressure during the bonding process. On the contrary, the uniform Au layer can be seen in Fig. 1b. The results of EDX (Table 1) illustrate that the whole Au layer has been converted to the Au–Al IMCs and no significant changes will generate during aging in the first case. Nevertheless, IMCs emerge only near the Al side and grow rapidly during aging in the latter case.

On the one hand, the primary Au–Al IMCs formed in the bonding process grow with the increasing aging time. Figure 2 performs the IMCs evolution of bonding joints annealing at 125 $^{\circ}\text{C}$ for 24 h, 120 h, 240 h and 360 h. First, the small punctate IMCs (Fig. 2a) transform into bulky IMCs (Fig. 2b) with the aging time prolonging. There is a crack on the interface between Al and Au phase in the meantime. Then, the bulky IMCs grow transversely resulting in the formation of lamellar IMCs (Fig. 2c). Finally, the flaws

Table 1 EDX results for point 1–15 in Au–Al bonds

| Points | Al K at % | Cu K at % | Au L at % |
|--------|-----------|-----------|-----------|
| 1 | 75.73 | 3.38 | 20.89 |
| 2 | 26.78 | 12.81 | 60.41 |
| 3 | 12.07 | 63.71 | 24.22 |
| 4 | 16.01 | – | 83.99 |
| 5 | – | 6.23 | 93.77 |
| 6 | – | 19.71 | 80.29 |
| 7 | 23.52 | 2.67 | 73.81 |
| 8 | – | 5.14 | 94.86 |
| 9 | – | 11.29 | 88.71 |
| 10 | 22.26 | 3.11 | 74.64 |
| 11 | 22.34 | 3.58 | 74.08 |
| 12 | 29.72 | 4.81 | 65.47 |
| 13 | 32.76 | 2.18 | 65.06 |
| 14 | 77.51 | 1.25 | 21.23 |
| 15 | 2.34 | 7.96 | 89.70 |

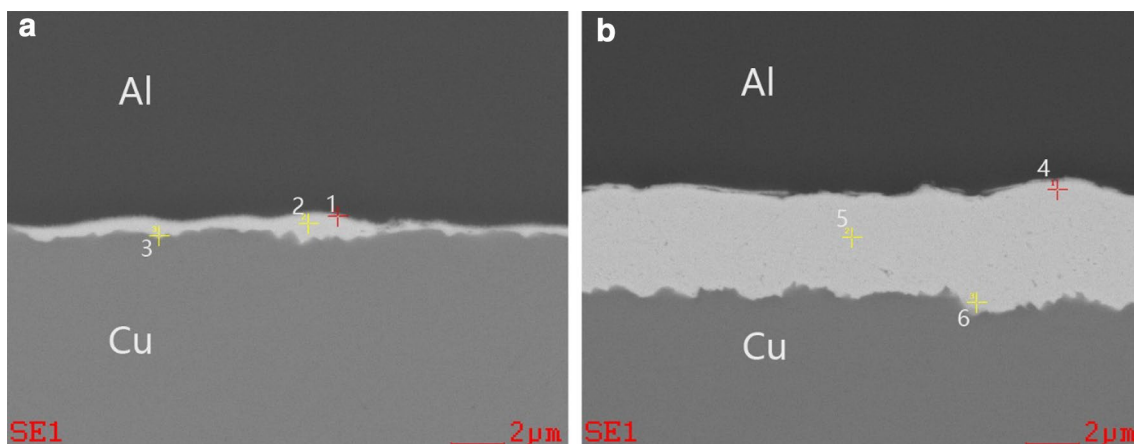


Fig. 1 SEM images of two typical regions on the interface of initial Au–Al bonds

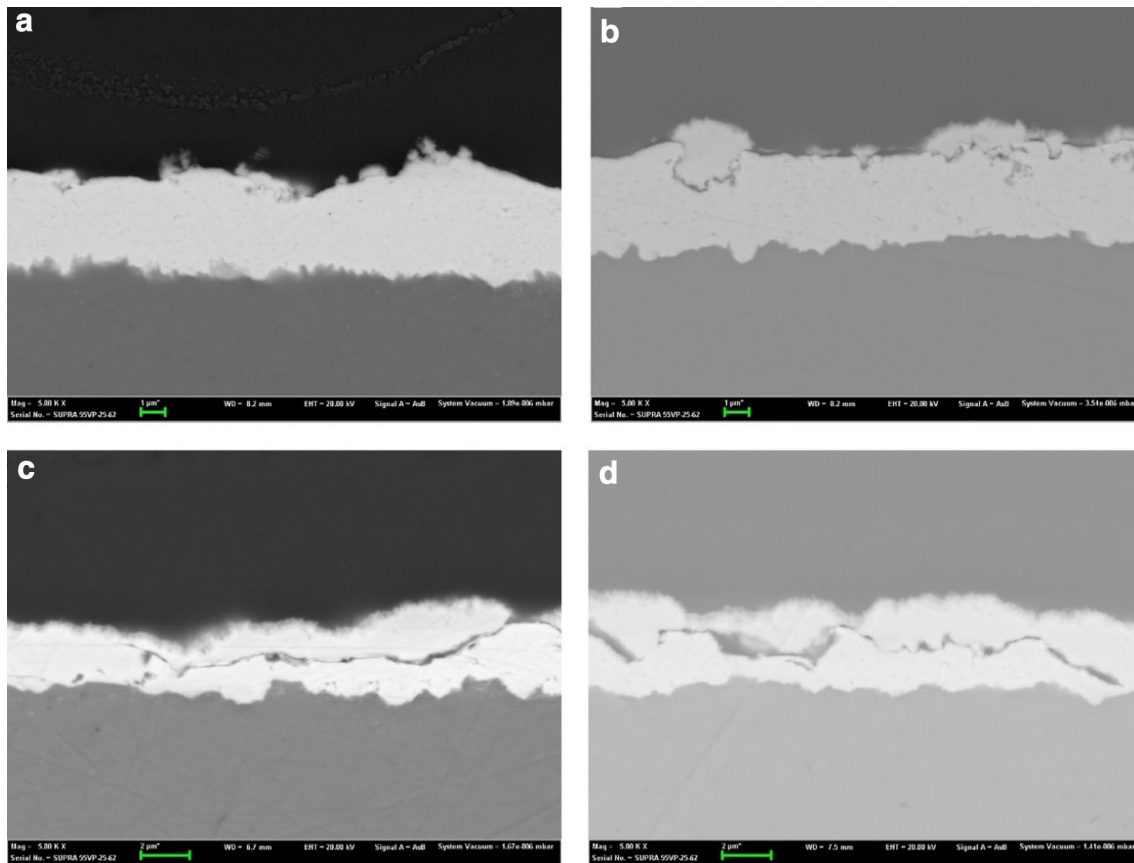


Fig. 2 SEM images of Au–Al bonds after aging **a** 24 h, **b** 120 h, **c** 240 h, **d** 360 h at 125 °C

and IMCs grow continuously (Fig. 2d). On the other hand, ambient temperature is also vital for IMCs growth. Figure 3 shows the Au–Al bonds after aging 240 h under different temperatures. With the increasing aging temperature, the thickness of IMC rises gradually, and the cracks become larger. Especially, multilayer IMCs are found in Fig. 3c. Five types of IMCs including Au_4Al , Au_2Al , Au_8Al_3 , AuAl and AuAl_2 possibly exist based on the equilibrium phase diagram of Au–Al [14]. EDX was applied (Fig. 4) to examine the compositions of IMCs and the results are listed in Table 1. The contents of points 7, 10 and 11 indicate the existence of Au_4Al near the Au layer, and the components of point 14 suggest the formation of AuAl_2 along Al side, which is consistent with Xu et al. [15, 16]. The components of points 12 and 13 predict that a mixed phase consisted of Au_8Al_3 and Au_2Al is located between AuAl_2 and Au_4Al layer. The mechanic properties of IMCs are further computed by the first-principles calculations. A stress–strain method [17] was utilized to calculate the elastic matrices C_{ij} of the Au–Al IMCs. The loaded strains on equilibrium lattice ranging from -0.2 to 0.2% with a step of 0.005% determine the changes of total energy. However, the strains are loaded in different ways for the variety of lattice structure, causing the diversity

of elastic matrices which are displayed in Table 2. The polycrystalline elastic modulus [bulk modulus (K), shear modulus (G) and Young's modulus (E)] and Poisson's ratio ν are enumerated in Table 3, which are deduced from the values of C_{ij} based on the Voight–Reuss–Hill approximation [18, 19]. The properties of Au–Al IMCs are quite different from the initial metal. Especially, the Young's modulus of Au_2Al (111.04 GPa) and AuAl_2 (111.56 GPa) are particularly high, indicating the high brittleness.

3.2 Formation of cracks

We find that the cracks expand with the growth of IMC on the Al/Au interface, which are attributed to the Kirkendall effect [20], volumetric shrinkages [21] and thermal mismatch. In Au–Al system, the diffusion constant for Au atoms spreading to Al metal is five orders of magnitude than the inverse diffusion [22]. Consequently, the Au atoms quickly diffuse to the Al metal, forming the Kirkendall voids which will turn into cracks during aging. Besides, Xu et al. [21] estimated that the intermetallic growth and phase transformation will result in volumetric shrinkage in Au–Al bonds. During aging, significantly volumetric shrinkage arising

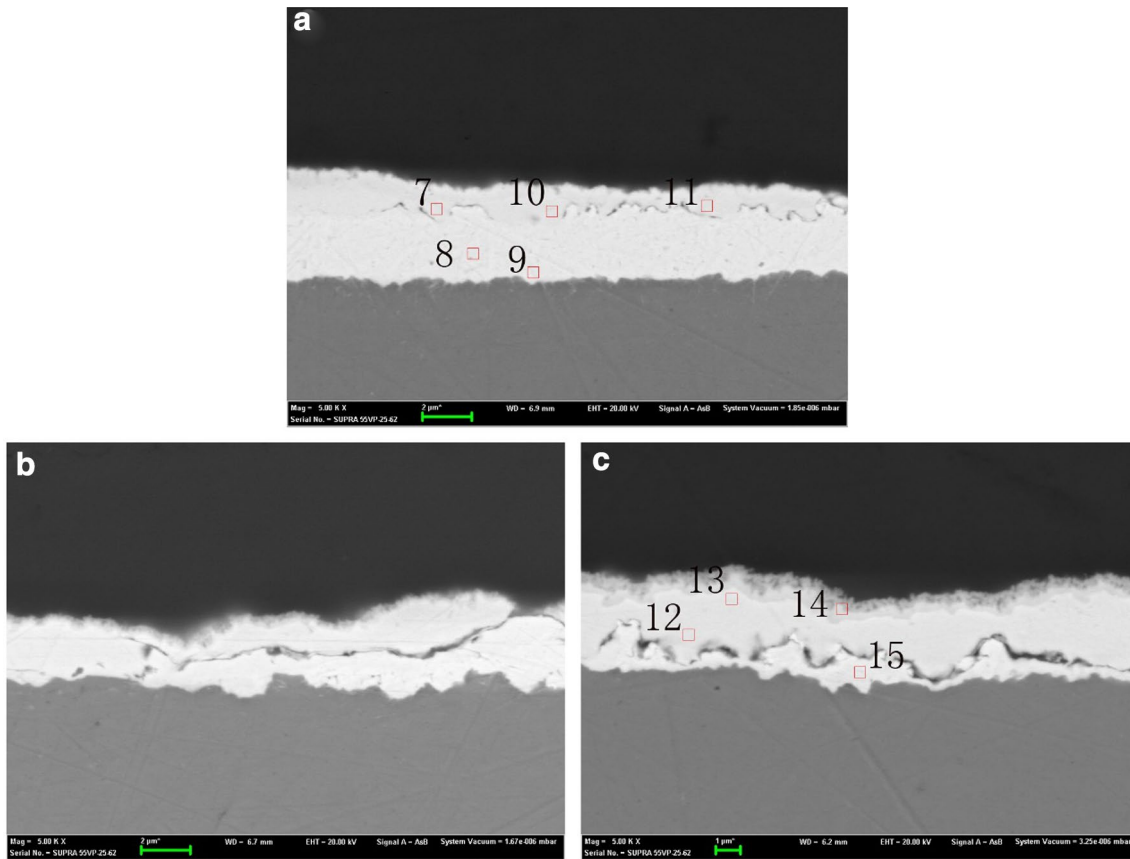


Fig. 3 SEM images of Au–Al bonds after aging 240 h at **a** 100 °C, **b** 125 °C, **c** 150 °C

from rapid growth of IMCs develops large plastic stress [23] in IMCs, which is contributed to the expansion of cracks. The thermal expansion is controlled by the anharmonic effect of lattice vibration, signifying that the bonding force between atoms determines the coefficient of thermal expansion (CTE). Meanwhile, Young's modulus also depends on the atomic bonding force [24]. From the calculation results of Au–Al IMC, the CTE mismatch will occur after thermal aging. Hence, the cracks are easily formed at the interface between Au and IMC layer.

3.3 Reliability assessment

Along with the expansion of cracks, the growth of IMCs, makes the performance of bonding joints degenerate. Therefore, the thickness of IMCs layer is considered as the characteristic parameter to evaluate the degradation degree. We have measured the IMCs thickness of three bonds, and the results of the measurement are printed in Table 4. Under the premise of fixed thermal aging temperature, the growth kinetics of IMCs layer can be estimated using the diffusion equation [25, 26],

$$H - H_0 = \sqrt{Dt} \quad (1)$$

where H is the thickness of IMCs layer, H_0 is the initial thickness, t means the aging time, D represents the diffusion constant. For curve fitting, the diffusion equation is rewritten as following,

$$Y = AX + B \quad (2)$$

where $Y = H$, $A = \sqrt{D}$, $X = \sqrt{t}$ and $B = H_0$. This equation is individually fitted to the growth paths of IMCs layer at each temperature level. The fitting results are plotted in Fig. 4, and the coefficient estimated in diffusion equation of bond 1 are summarized in Table 5. It can be found that the diffusion constants increase with the aging temperature rising. In experiment, the diffusion constant of Au/Al system was found to be $2.2E-18 \text{ m}^2/\text{s}$ at the temperature of 130 °C [27]. In our estimation, the diffusion constant is $2.832E-18 \text{ m}^2/\text{s}$ at 125 °C which is consistent with the experimental data proving the credibility of this diffusion equation.

The failure time is the time when the actual degradation path reaches the prespecified critical degradation level

Fig. 4 Fits of diffusion equation to the thermal aging data at **a** 100 °C, **b** 125 °C, **c** 150 °C

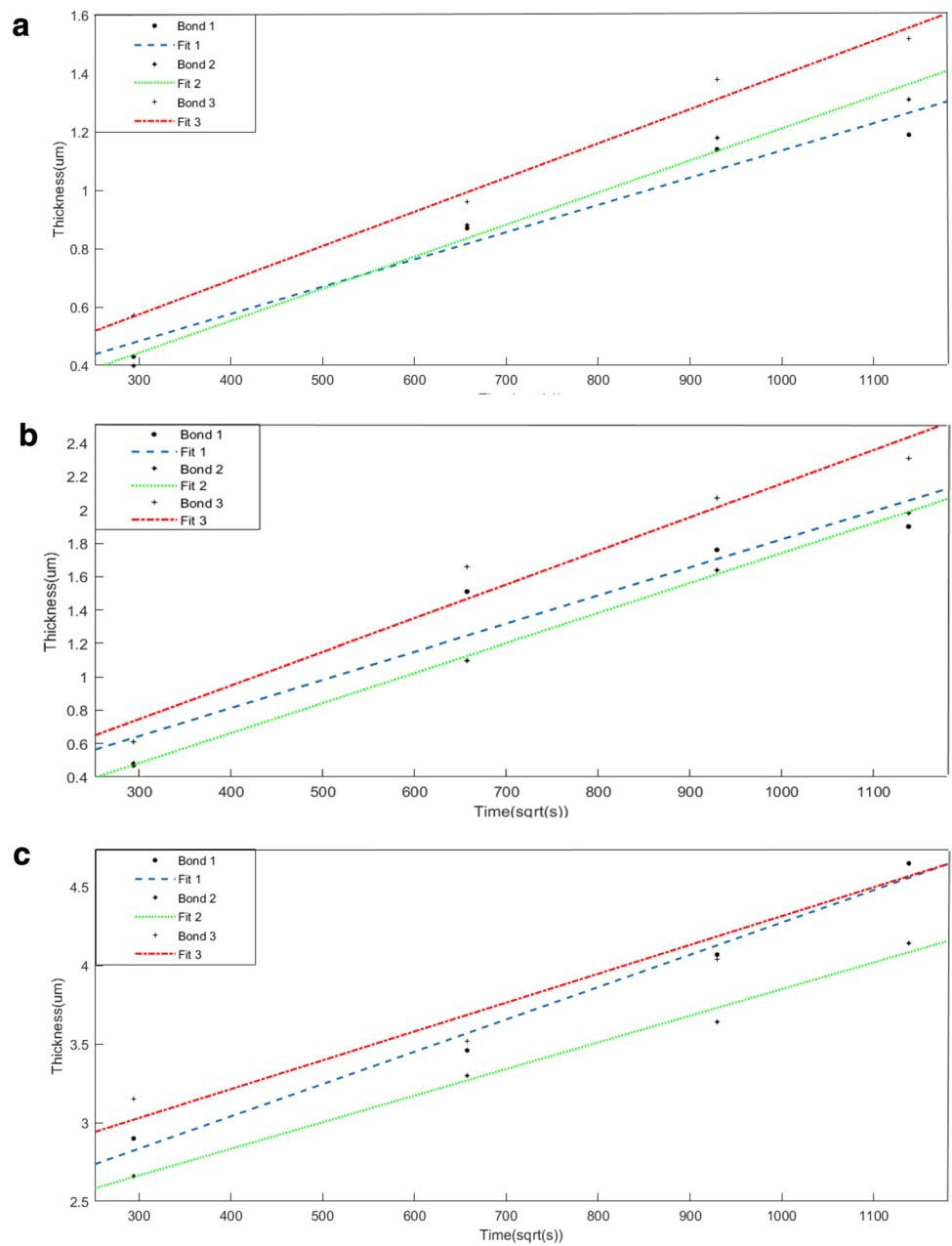


Table 2 The calculated elastic constants of Au–Al IMCs

| IMCs | C_{11} GPa | C_{22} GPa | C_{33} GPa | C_{44} GPa | C_{55} GPa | C_{66} GPa | C_{12} GPa | C_{13} GPa | C_{23} GPa |
|--------------------|-----------------|-----------------|-----------------|-----------------|-----------------|-----------------|-----------------|-----------------|-----------------|
| Au ₄ Al | 138.41 | 138.41 | 138.41 | 26.52 | 26.52 | 26.52 | 122.46 | 122.46 | 122.46 |
| Au ₂ Al | 184.61 | 158.87 | 202.22 | 39.59 | 41.79 | 36.70 | 84.34 | 89.23 | 102.15 |
| AuAl ₂ | 134.45 | 134.45 | 134.45 | 65.41 | 65.41 | 65.41 | 90.86 | 90.86 | 90.86 |

during aging. In this study, we defined the failure time as the time when the thickness of IMC layer reaches 3 μm on account of the depletion of the initial 3-μm-thick Au layer. We predict the failure time using the diffusion equation because the IMCs layer did not reach the failure level at

100 °C and 125 °C. The estimated failure times at each temperature are summarized in Table 6 for lifetime prediction.

From the diffusion equation, we get the failure times of each thermal stress. A relationship should be built between each temperature level and failure time to extrapolate the lifetime

Table 3 The calculated mechanical properties of Au–Al IMCs

| IMCs | <i>K</i> /GPa | <i>G</i> /GPa | <i>E</i> /GPa | ν |
|--------------------|---------------|---------------|---------------|-------|
| Au ₄ Al | 127.77 | 16.42 | 47.24 | 0.44 |
| Au ₂ Al | 121.06 | 41.21 | 111.04 | 0.35 |
| AuAl ₂ | 105.39 | 42.14 | 111.56 | 0.32 |
| Au | 137.33 | 14.67 | 42.49 | 0.45 |
| Al | 83.33 | 23.92 | 65.50 | 0.37 |

Table 4 The thickness of IMCs layer in thermal aging

| Temperature/°C | Thickness/ μm | Time/h | | | |
|----------------|--------------------------|--------|------|------|------|
| | | 24 | 120 | 240 | 360 |
| 100 | Bond 1 | 0.43 | 0.87 | 1.14 | 1.19 |
| | Bond 2 | 0.40 | 0.88 | 1.18 | 1.31 |
| | Bond 3 | 0.57 | 0.96 | 1.38 | 1.52 |
| 125 | Bond 1 | 0.47 | 1.51 | 1.76 | 1.90 |
| | Bond 2 | 0.48 | 1.10 | 1.64 | 1.98 |
| | Bond 3 | 0.61 | 1.66 | 2.07 | 2.31 |
| 150 | Bond 1 | 2.90 | 3.46 | 4.07 | 4.65 |
| | Bond 2 | 2.66 | 3.30 | 3.64 | 4.14 |
| | Bond 3 | 3.15 | 3.52 | 4.04 | 4.75 |

Table 5 Parameters estimated in diffusion equation at each temperature

| Temperature (°C) | 100 | 125 | 150 |
|----------------------------------------------|-----------|-----------|-----------|
| Value of <i>A</i> | 9.327E–10 | 1.683E–9 | 2.055E–9 |
| Value of <i>B</i> | 2.035E–7 | 1.396E–7 | 2.219E–6 |
| Diffusion constant (m^2/s) | 8.699E–19 | 2.832E–18 | 4.223E–18 |

Table 6 The estimated failure time at of three bonds at each temperature

| Temperature (°C) | 100 | 125 | 150 |
|------------------|--------|-------|------|
| Bond 1 | 2497 h | 802 h | 40 h |
| Bond 2 | 1919 h | 804 h | 69 h |
| Bond 3 | 1561 h | 559 h | 23 h |

under normal use condition or every interesting stress level. Weibull distribution [28], as the popular lifetime distribution in reliability test, is selected in the present study for the universality of its shape, especially the well-fitting with the lifetime distribution of electronic equipment. And the cumulative failure function can be written as following,

$$F(t) = 1 - \exp \left[- \left(\frac{t}{\eta} \right)^m \right] \quad (t, m, \eta > 0) \quad (3)$$

where t is the time, η is the scale parameter, m is the shape parameter determining the structure of the distribution curve. The shape parameter is closely related to the failure mechanism of bonding joints. That is, different value of shape parameter results in variety of failure rate. When the m is greater than, less than and equal to 1, the Weibull distribution has the increasing, decreasing and constant failure rate, respectively. The growth rate of IMCs increases with the aging temperature ascending which indicates the value of m is more than 1. In addition, we assume the invariance of m because of the changeless failure mechanism in all thermal stress level. The scale parameter is also called characteristic life (the failure probability is 63.2% at this time) which has a relationship with thermal stress. For reliability test, there are many typical physical stresses such as temperature, mechanism load, voltage and humidity. These stresses all have the corresponding acceleration model used to describe the effects on the lifetime. The Arrhenius acceleration model is generally employed to describe the relationship between temperature and characteristic life. It can be presented as [29],

$$\eta = A \exp \left(\frac{E}{kT} \right) \quad (4)$$

where E is the activation energy, k is the Boltzmann's constant ($8.6171\text{E}-5 \text{ eV}/^\circ\text{C}$), A is the non-thermal constant and T is the absolute Kelvin temperature.

For the purpose of lifetime prediction under normal use condition, the Weibull–Arrhenius [30] model is constructed according the relation between the characteristic life and thermal stress as,

$$F(t) = 1 - \exp \left[- \left(\frac{t}{A \exp \left(\frac{E}{kT} \right)} \right)^m \right] \quad (t, m, \eta > 0) \quad (5)$$

Using the estimated failure lifetime of each temperature, the parameters of Weibull–Arrhenius model can be evaluated by the double logarithm linear method. The logarithm of the formula (5) is taken twice as following,

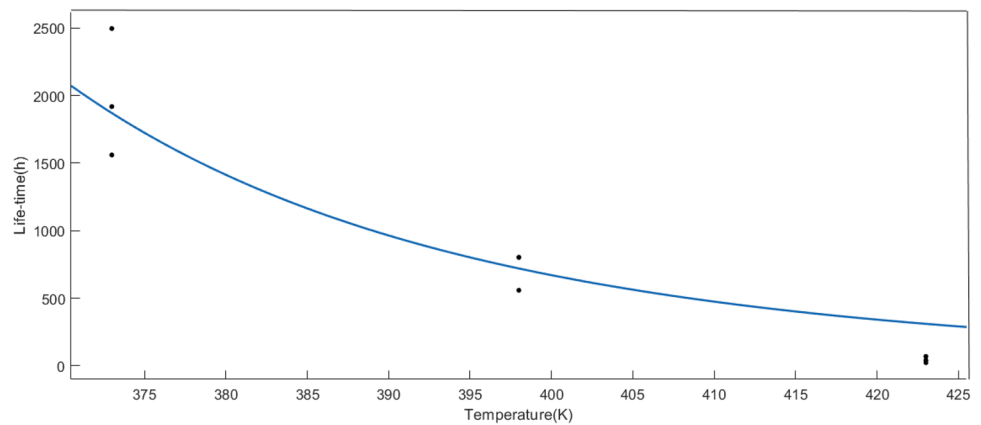
$$\ln \ln \frac{1}{1 - F(t)} = m \left[\ln(t) - \ln A - \frac{E}{kT} \right] \quad (6)$$

When the failure data is little, it is incorrect to replace the frequency with probability. In this study, we utilize the median rank estimation method to estimate the cumulative failure probability, which is given by,

$$F(t_i) = \frac{i - 0.3}{n + 0.4} \quad (7)$$

where n is the total number of samples, i is the number of failures at t_i time. For the aim to predict the lifetime of the

Fig. 5 Fit of the Weibull-Arrhenius model to the lifetime at each temperature



bonding joints under normal use condition, Eq. (6) is rewritten as,

$$t = A \exp\left(\frac{-\ln \ln(1 - F(t))}{m}\right) \exp\left(\frac{E}{kT}\right) \quad (8)$$

The parameters of this model are evaluated according to the failure data in thermal aging. The estimated results are plotted in Fig. 5, and the values of m , A and $\frac{E}{k}$ are 352.1, $4.710\text{E}-4$ and 5668, respectively. Assuming the working temperature is $25\text{ }^{\circ}\text{C}$, the estimated lifetime of the bonding joints is 85,730 h (9.79 years). The remaining life also can be obtained by subtracting the actual service life from the predicted lifetime under the working temperature.

4 Conclusion

In this work, we found two typical regions in Au–Al bonding joints using parallel gap resistance microwelding for the difference of bonding pressure. In one case, there is a uniform Au layer. In another case, the Au layer has a tremendous deformation. In the first case, the behavior of IMCs was investigated under thermal aging. The punctate IMCs grow into bulky IMCs and finally become lamellar IMCs with time increasing. The lamellar IMCs are multilayer IMCs including Au_4Al , AuAl_2 , Au_2Al and Au_8Al_3 . For further understanding, the IMCs, the first-principle calculations were performed, finding the notable mechanical changes between initial metals and IMCs. There is a crack at the interface between IMCs and Au layer, which is attributed to the combination of the Kirkendall effect, volumetric shrinkages and thermal mismatch. Assuming that the failure threshold of bonding joints is the thickness of IMC layer reaching $3\text{ }\mu\text{m}$, the lifetimes are estimated from the diffusion equation. To extrapolate the lifetime under normal use condition, the Weibull–Arrhenius is introduced, and the estimated lifetime at $25\text{ }^{\circ}\text{C}$ is 9.79 years.

Acknowledgements This work was supported by the National Natural Science Foundation of China (51572190).

References

1. S.A. Gam, H.J. Kim, J.S. Cho et al., Effects of Cu and Pd addition on Au bonding wire/Al pad interfacial reactions and bond reliability. *J. Electron. Mater.* **35**(11), 2048–2055 (2006)
2. Z.W. Zhong, Overview of wire bonding using copper wire or insulated wire. *Microelectron. Reliab.* **51**(1), 4–12 (2011)
3. P. Liu, L. Tong, J. Wang et al., Challenges and developments of copper wire bonding technology. *Microelectron. Reliab.* **52**(6), 1092–1098 (2012)
4. C.D. Breach, F.W. Wulff, A brief review of selected aspects of the materials science of ball bonding. *Microelectron. Reliab.* **50**(1), 1–20 (2010)
5. T.C. Wei, A.R. Daud, Mechanical and electrical properties of Au–Al and Cu–Al intermetallics layer at wire bonding interface. *J. Electron. Packag.* **125**(4), 617–620 (2003)
6. Y. Liu, Y. Tian, B. Liu et al., in *Interconnection of Cu wire/Au plating pads using parallel gap resistance microwelding process*. 2016 17th International Conference on Electronic Packaging Technology. (IEEE, 2016), p. 43–46.
7. R.P. Sharma, P.K. Khanna, D. Kumar et al., in *Development and analysis of noble-metal wire interconnections on Au thick film using parallel gap welding technique for MEMS and microsystems*. 2008 International Conference on Recent Advances in Microwave Theory and Applications. (IEEE, 2008), p. 739–741
8. M.I. Khan, J.M. Kim, M.L. Kuntz et al., Bonding mechanisms in resistance microwelding of 316 low-carbon vacuum melted stainless steel wires. *Metall. Mater. Trans. A* **40**(4), 910–919 (2009)
9. J.E. Martinez, L.B. Johannes, D. Gonzalez et al., Metallography of battery resistance Spot Welds. *Microsc. Microanal.* **21**(S3), 2427–2428 (2015)
10. Z. Chen, Joint formation mechanism and strength in resistance microwelding of 316L stainless steel to Pt wire. *J. Mater. Sci.* **42**(14), 5756–5765 (2007)
11. M.O. Alam, H. Lu, C. Bailey et al., Fracture mechanics analysis of solder joint intermetallic compounds in shear test. *Comput. Mater. Sci.* **45**(2), 576–583 (2009)
12. G. Kresse, J. Furthmüller, Efficient iterative schemes for ab initio total-energy calculations using a plane-wave basis set. *Phys. Rev. B* **54**(16), 11169 (1996)

13. Y. Tian, W. Zhou, P. Wu, A density functional investigation of the structural, elastic and thermodynamic properties of the Au–Sn intermetallics. *J. Electron. Mater.* **45**(1), 639–647 (2016)
14. J.L. Murray, H. Okamoto, T.B. Massalski, The Al–Au (aluminum–gold) system. *Bull. Alloy Ph. Diagr.* **8**(1), 20–30 (1987)
15. H. Xu, C. Liu, V.V. Silberschmidt et al., Intermetallic phase transformations in Au–Al wire bonds. *Intermetallics* **19**(12), 1808–1816 (2011)
16. H. Xu, C. Liu, V.V. Silberschmidt et al., A micromechanism study of thermosonic gold wire bonding on aluminum pad. *J. Appl. Phys.* **108**(11), 113517 (2010)
17. S.Q. Wang, H.Q. Ye, Ab initio elastic constants for the lonsdaleite phases of C, Si and Ge. *J. Phys.: Condens. Matter* **15**(30), 5307 (2003)
18. J.H. Westbrook, R.L. Fleischer, *Basic Mechanical Properties and Lattice Defects of Intermetallic Compounds* (Wiley, Chichester, 2000)
19. R. Hill, The elastic behaviour of a crystalline aggregate. *Proc. Phys. Soc. A* **65**(5), 349 (1952)
20. H. Springer, A. Kostka, J.F. Dos Santos et al., Influence of intermetallic phases and Kirkendall-porosity on the mechanical properties of joints between steel and aluminium alloys. *Mater. Sci. Eng. A* **528**(13–14), 4630–4642 (2011)
21. H. Xu, C. Liu, V.V. Silberschmidt et al., New mechanisms of void growth in Au–Al wire bonds: volumetric shrinkage and intermetallic oxidation. *Scripta Mater.* **65**(7), 642–645 (2011)
22. G. Neumann, C. Tuijn, *Self-diffusion and Impurity Diffusion in Pure Metals: Handbook of Experimental Data* (Elsevier, Amsterdam, 2011)
23. G.B. Stephenson, Deformation during interdiffusion. *Acta Metall.* **36**(10), 2663–2683 (1988)
24. L. Shen, A.Q. Foo, S. Wang et al., Enhancing creep resistance of SnBi solder alloy with non-reactive nano fillers: a study using nanoindentation. *J. Alloys Compd.* **729**, 498–506 (2017)
25. J. Shen, Y.C. Chan, S.Y. Liu, Growth mechanism of Ni₃Sn₄ in a Sn/Ni liquid/solid interfacial reaction. *Acta Mater.* **57**(17), 5196–5206 (2009)
26. A.K. Gain, Y.C. Chan, Growth mechanism of intermetallic compounds and damping properties of Sn–Ag–Cu–1 wt% nano-ZrO₂ composite solders. *Microelectron. Reliab.* **54**(5), 945–955 (2014)
27. C. Weaver, D.T. Parkinson, Diffusion in gold–aluminium. *Philos. Mag.* **22**(176), 377–389 (1970)
28. H. Rinne, *The Weibull Distribution: A Handbook* (Chapman and Hall/CRC, Boca Raton, 2008)
29. S.J. Bae, S.J. Kim, J.I. Park et al., Lifetime prediction through accelerated degradation testing of membrane electrode assemblies in direct methanol fuel cells. *Int. J. Hydrogen Energy* **35**(17), 9166–9176 (2010)
30. R.M. Dahlquist-Willard, M.N. Marshall, S.L. Betts et al., Development and validation of a Weibull-Arrhenius model to predict thermal inactivation of black mustard (*Brassica nigra*) seeds under fluctuating temperature regimens. *Biosyst. Eng.* **151**, 350–360 (2016)

Publisher's Note Springer Nature remains neutral with regard to jurisdictional claims in published maps and institutional affiliations.